THE ASTRONOMICAL JOURNAL, 161:160 (17pp), 2021 April https://doi.org/10.3847/1538-3881/abde4c

The Binary INformation from Open Clusters Using SEDs (BINOCS) Project: Reliable Photometric Mass Determinations of Binary Star Systems in Clusters

Benjamin A. Thompson[1,2], Peter M. Frinchaboy[1], Taylor Spoo[1], and John Donor[1]
[1] Department of Physics & Astronomy, Texas Christian University, TCU Box 298840, Fort Worth, TX 76129, USA; p.frinchaboy@tcu.edu, t.spoo@tcu.edu, j.donor@tcu.edu
[2] GitHub, Inc., USA

Received 2019 October 3; revised 2021 January 19; accepted 2021 January 19; published 2021 March 3

Abstract

We introduce a new binary detection technique, BINARY INFORMATION FROM OPEN CLUSTERS USING SEDS (BINOCS), which we show is able to determine reliable stellar multiplicity and masses over a much larger mass range than current approaches. This new technique determines accurate component masses of binary and single systems of the open clusters' main sequence by comparing observed magnitudes from multiple photometric filters to synthetic star spectral energy distributions (SEDs), allowing us to systematically probe the binary population for *low-mass* stars in clusters for eight well-studied open clusters. We provide new deep, infrared photometric catalogs (1.2–8.0 μm) for the key open clusters NGC 1960 (M36), NGC 2099 (M37), NGC 2420, and NGC 2682 (M67), using observations from NOAO/NEWFIRM and Spitzer/IRAC. Using these deep multiwavelength catalogs, the BINOCS method is applied to these clusters to determine accurate component masses for *unresolved* cluster binaries. We explore binary fractions as a function of cluster age, Galactic location, and metallicity.

Unified Astronomy Thesaurus concepts: Open star clusters (1160); Binary stars (154); Infrared photometry (792)

Supporting material: machine-readable table

1. Introduction

Binary stars have long been recognized to have an effect on stellar evolution, allowing the formation of nonstandard stars, such as blue stragglers. While these stars may be formed in the field, their abundance in star clusters leads us to explore the effects of environment on the frequency of these stars. Additionally, it has long been recognized that the frequency of binaries will also affect the long-term dynamics and stellar distributions within a cluster.

In order to more fully understand these effects on stellar and cluster evolution, the number of binaries within a cluster must be accurately determined, as well as other properties about the binary population. Having these data will allow correlations to be made between properties of the binary sample and dynamical traits of the cluster, as well as the frequency of anomalous stars. Correctly determining the number and composition of binary systems will allow deeper understanding of the physical processes behind stellar and cluster evolution.

Internal processes can result in stars being ejected from the cluster owing to gravitational interaction with other member stars. When a less massive star gravitationally interacts with a more massive one, it may pick up enough energy to be accelerated beyond the escape velocity of the cluster. Binary systems may amplify this process by contributing part of their orbital energy to interactions, which is usually greater than the kinetic energy of the system moving through the cluster, which is fairly easy in poorly bound, low-mass, low-dispersion systems like open clusters.

Due to the vast timescale over which clusters evolve, stellar ejection cannot be studied observationally. Cluster ejection is usually studied via detailed *N*-body simulations (Hurley et al. 2001, 2005), which can give a detailed description of what stars were ejected, when they were ejected, and how fast they were moving at the time of ejection. Each of these parameters dictates how the field population of the galaxy may have been built up by open cluster dissolution.

N-body simulations have already been run to analyze the binary population's effect on escaping stars, discovering only a slight difference when varying the cluster binary percentage from 0% to 70% (Moyano Loyola & Hurley 2013). These studies have made assumptions about the primordial binary population, however, such as an even mass ratio (ratio of larger to smaller star mass) distribution, which may not be the case in reality.

Measuring the cluster binary fraction and mass ratio distribution (as a function of primary mass) for real clusters will go a long way in calibrating these *N*-body simulations. Analyzing open clusters with various ages will also allow *N*-body simulations to check intermediate steps against these "benchmarks," further improving their accuracy and predicting power.

It has also long been established that members of star clusters experience mass segregation. Binary systems, on average, are more massive than single stars and have generally been thought to become more centrally concentrated than singles owing to the same mechanism. A decreasing binary fraction with radius, indicative of mass segregation, has been observationally confirmed for several open and globular clusters (e.g., Geller & Mathieu 2012; Milone et al. 2012). Similar analyses have been conducted on the young (15–30 Myr), massive cluster NGC 1818, located in the Large Magellanic Cloud (LMC), producing conflicting results, which having more detailed clusters with binary characterization will allow us to fully explore.

While the advent of high-precision photometry, from Kepler and TESS, has opened up new studies for analyzing eclipsing binary systems, systematic methods for reliably and efficiently probing cluster binary populations for large numbers of clusters have remained elusive.

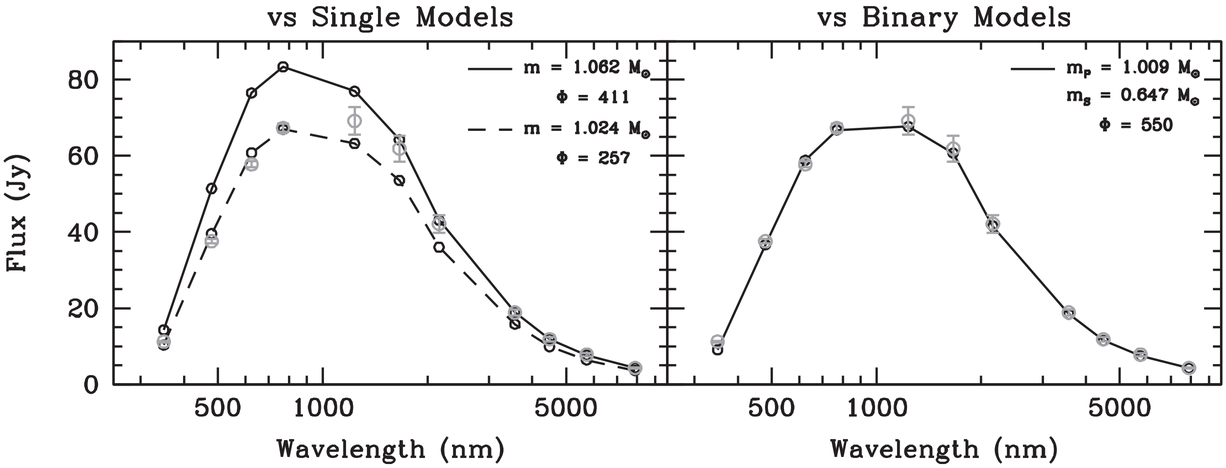

Figure 1. SED fitting of the observed star in NGC 2682. Left: comparison of observed fluxes (gray dots) to best-fit single-star model SEDs. Right: comparison of observed fluxes to best-fit single model. For each model, the fit's Φ value, defined in Section 2.3, is shown.

2. Binary Detection

2.1. Previous Large-scale Methods in Clusters

Currently, binary systems within open clusters are detected using one of two methods. The first is *two-band detection*, leveraged by both Elson et al. (1998) and de Grijs et al. (2013), which uses a cluster color–magnitude diagram (CMD) to quickly separate stars into singles and binaries. Stars lying far enough from the cluster single-star main sequence are classified as binaries, while all others are deemed single stars. While this method is quick and easy (only requiring imaging in two filters), it is plagued by degeneracies when attempting to determine accurate masses. In their paper, de Grijs et al. admit that this method will only work inside a small mass range of NGC 1818. Outside of this region "the CMD is too steep to easily disentangle single from binary stars and blends. In addition, toward fainter magnitudes, photometric errors start to dominate any potential physical differences." To explore radial distributions of binary systems with a wide range of masses, two-band detection is not feasible.

The ideal method for this work is using radial velocity (RV) measurements to determine stellar multiplicity, as this approach will yield the most information about each system. There are, however, significant drawbacks: due to the number of stars in each cluster and the velocity precision necessary to detect most binary systems, RV surveys can take hundreds of nights over many years, if not decades, to complete. Additionally, RV surveys cannot accurately measure cluster stars fainter than $V \sim 16$ without significant observing time on large telescopes, which removes a majority of cluster stars from the RV studies conducted so far.

With the growth of large-scale, space- and ground-based photometric surveys (e.g., Pan-STAARS, ESA Gaia, LSST, Two Micron All Sky Survey (2MASS), UKIDSS, VVV, *Roman* Space Telescope, Spitzer/GLIMPSE, WISE; Chambers et al. 2016; Gaia Collaboration et al. 2016; Ivezić et al. 2019; Skrutskie et al. 2006; Lucas et al. 2008; Minniti et al. 2010; Spergel et al. 2013; Churchwell et al. 2009; Wright et al. 2010), another photometry method would be ideal that is not cost-prohibitive in terms of telescope time but also yields accurate and detailed binary information over a wide range of stellar masses.

2.2. BINOCS

We introduce the new BINARY INFORMATION FROM OPEN CLUSTERS USING SEDS (BINOCS) binary detection method, which determines accurate component masses of binary and single systems within open clusters by comparing observed magnitudes from multiple photometric filters to synthetic star spectral energy distributions (SEDs). An example of this method is shown in Figure 1.

A star in NGC 2682 was observed in 11 bands ($ugriJHK_S$ [3.6][4.5][5.8][8.0]).[3] When the observed magnitudes are compared against all single-star model SEDs, two close-fitting models are detected; however, neither fits the entire spectrum well (left panel of Figure 1). While one model (with a mass of 1.062 $M_\odot$) fits accurately in the optical and J band, it diverges for IR fluxes. The 1.024 $M_\odot$ model fits oppositely: overestimating optical fluxes, while accurately mapping the IR.

Next, the star is compared to binary model SEDs, where the best fit is much more accurate (right panel of Figure 1). A binary star in NGC 2682 with a primary mass of 1.009 $M_\odot$ and secondary mass of 0.647 $M_\odot$ fits within the observational uncertainties for 10 of the 11 observed bands. This star, while classified as a "single" in a previous RV study (Mathieu & Latham 1986), is matched much more closely as a binary system using the BINOCS approach. Possible reasons for this mismatch will be further discussed in Section 7.

A similar but different Bayesian-based analysis has also recently been introduced by Cohen et al. (2020).

2.3. BINOCS Code

This BINOCS detection method is implemented through a publicly available code.[4] The steps implemented by this code are described below.

First, the BINOCS code creates a library of synthetic cluster star SEDs using an isochrone, which lists stellar parameters ($T_{\rm eff}$, $\log g$) and absolute magnitudes for a model star, given a cluster age, metallicity, reddening,[5] and stellar mass. Isochrone sets often come in coarse mass grids, which hampers the BINOCS code's ability to compute accurate mass estimates.

---

[3] IRAC [5.8] and [8.0] magnitudes provide little strength to the fit since they are on the Rayleigh–Jeans tail of the SED, and they are significantly more shallow than the [3.6] and [4.5] magnitudes; thus, while they were used in testing the technique, we choose not to use them in the analysis presented here.

[4] http://github.com/bathompso/binocs

[5] The method works well over a range of reddening but would be significantly adversely affected by *differential* reddening, which we plan to improve in future versions of the BINOCS code.

Stellar parameters are interpolated cubically in mass, generating new isochrone points in steps of 0.01 $M_\odot$. This interpolation only works along the main sequence, however, where mass increases monotonically. For evolved stars, at the turnoff or red giant branch, the original isochrone points are used.

Using the new mass-interpolated isochrone model, SEDs are created by computing up to 15 filter magnitudes ($UBVRIugrizJHK_S$[3.6][4.5]) for every possible combination of single synthetic stars in an isochrone. The isochrone absolute magnitudes are then adjusted to observed apparent magnitudes using the cluster's distance and reddening.

Next, each star in the cluster is compared to every possible model (binary and single) using

$$\Phi = \sum_{\rm filters} \frac{1}{|m_{\rm star} - m_{\rm model}| + \eta_{\rm soft}}. \tag{1}$$

Here $m_{\rm star}$ is the observed magnitude of the star in a particular band, while $m_{\rm model}$ is the apparent magnitude of the synthetic model star. $\eta_{\rm soft}$ is a single global softening parameter for which we use $\eta_{\rm soft} = 0.01$ (mag), the typical uncertainty of the photometry.

If any of the sum elements is below a threshold value, e.g., $\frac{1}{|m_{\rm star} - m_{\rm model}| + \eta_{\rm soft}} < 10$ (meaning that the absolute difference in magnitudes is > 0.09), that element is declared to be "distant" and is not added to the sum. The selection of this threshold value is explored in Section 6.3. Only models with three good optical magnitudes ($UBVRIugriz$), three good near-IR magnitudes (JHK_S), and two good mid-IR magnitudes ([3.6][4.5]) are considered. Figure 1 illustrates why such a requirement is necessary: binary SEDs differ from those of single stars only when compared across a large wavelength range. In a small region, the differences between a binary and single SED are negligible. Requiring a minimum number of good filter magnitudes across the entire wavelength range will ensure that all models accurately fit the entire SED, not just a single portion of it.

After discarding those models with too many "distant" magnitudes, all Φ values are normalized by the number of "close" magnitudes used in the sum. The model with the highest Φ is chosen as the best fit. If no models have enough "close" magnitudes, the star is marked as a nonmember of the cluster.

After comparing each star to the full model library, it is also compared to only single models as a secondary check, using a much less stringent "close" magnitude cut—each sum element must be > 1. The purpose of this comparison is twofold: The first is to be able to compare best-fitting single and binary models for illustrative purposes, as shown in Figure 1. Second, some stars, while classified as binaries through the BINOCS method, are better classified as singles (these cuts will be explained in Section 6.4). If a star is forced to be classified as single, the parameters from this stage of fitting will be used to estimate its mass.

This fitting process is iterated 300 times, with each run randomly sampling magnitudes from a Gaussian distribution, with σ equal to the photometric uncertainty. After all 300 resamples, the BINOCS code determines whether the star is a member or not. If a majority of the chosen best fits denote that the star is a nonmember, then that star is declared to be a nonmember. Of the stars that are members, primary and secondary masses are determined by the median of all the best fits. Uncertainties in the mass estimates are computed using the standard deviation of all best-fit masses. Similarly for the single-only fitting runs, the best-fit mass and uncertainty are the median and standard deviation of all results, respectively.

Table 1

Adopted Cluster Parameters for All Clusters in the Data Set (Dias et al. 2002)

Cluster	Age (Gyr)	[Fe/H]	Dist (pc)	$E(B-V)$
NGC 188	6.30	−0.02	1820	0.06
NGC 1960 (M36)	0.03	⋯	1320	0.22
NGC 2099 (M37)	0.35	+0.08	1390	0.30
NGC 2158	1.10	−0.23	5080	0.36
NGC 2168 (M35)	0.13	−0.21	870	0.20
NGC 2420	2.00	−0.23	2500	0.03
NGC 2682 (M67)	3.50	+0.01	860	0.04
NGC 6791	8.00	+0.38	4170	0.15

By using multiple filters over a large wavelength range (0.3–4.5 μm), individual photometric errors become less important than in the two-band detection method. This means that the BINOCS method can determine mass information for stars outside of the small mass window available for two-band detection. Additionally, only a small amount of telescope time, relative to RV surveys, is needed to capture cluster photometry across the optical to mid-IR (assuming access to the correct observing facilities). This allows for the detection of binaries in many clusters using a minimum of resources.

Additionally, we initially tested this technique using only (0.3–2.2 μm) and found that the addition of the [3.6][4.5] significantly improved the resultant fitting, without utilizing the mid-IR filters, resulting in significantly larger fitting errors and greater uncertainty in distinguishing binarity.

Section 4 will cover the photometric data used by the BINOCS routine in this work, while Section 5 will discuss the underlying isochrone models used. Section 6 will explore the assumptions in the method description above (number of good filters necessary, number of resamples, magnitude threshold level). Section 7 will compare BINOCS results to those of previous RV studies of NGC 2168 and NGC 2682.

3. Cluster Sample

In total, eight clusters were targeted for use in this work. The distribution of cluster parameters for our targeted sample is shown in Table 1 and Figure 2.

The cluster sample covers a large area of the parameter space: ages range from 25 Myr to 9 Gyr, while [Fe/H] varies from −0.23 to +0.38%–40% to 200% the iron content of the Sun. Exploiting this parameter range is critical in answering the posed science questions. In reference to science question 1, there are three clusters with ages < 500 Myr. Using BINOCS results from these three clusters, an understanding of the primordial cluster binary population can be conceived.

4. Photometry Data

The BINOCS method requires photometric data over a wide range of the spectrum (optical to mid-IR) to detect binaries effectively. Photometric data over this range were compiled from a variety of sources listed in Table 2.

Table 2 summarizes the available data for use in this project, from the sources listed above, as well as from the literature. 2MASS, WISE, and IRAC data are available for all clusters

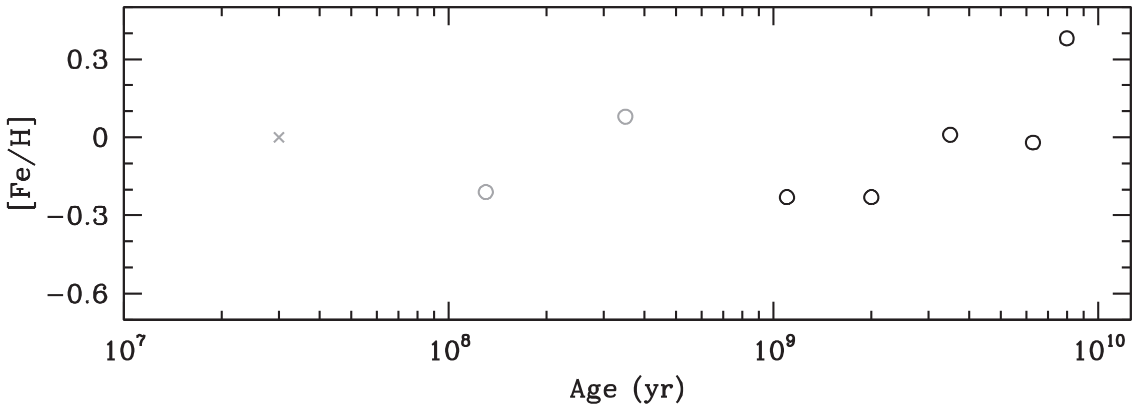

Figure 2. Distribution of the eight targeted clusters in age and [Fe/H] (Dias et al. 2002). The cross represents the cluster NGC 1960, which does not have any published metallicity information, so here we assume solar metallicity.

Table 2
Photometry Data for Clusters Analyzed in This Study

Cluster	Visual Data	Near-IR Data	Membership Data
NGC 188	von Hippel & Sarajedini (1998) Stetson et al. (2004)	2MASS	Geller et al. (2008) Platais et al. (2003)
NGC 1960 (M36)	MOSAIC	NEWFIRM	Sanner et al. (2000)
NGC 2099 (M37)	Hartman et al. (2008)	NEWFIRM	
NGC 2158	MOSAIC	2MASS	
NGC 2168 (M35)	MOSAIC	NEWFIRM	Geller et al. (2010)
NGC 2420	An et al. (2009)	NEWFIRM	
NGC 2682 (M67)	An et al. (2009) Yadav et al. (2008)	NEWFIRM	Mathieu et al. (1997) Yadav et al. (2008)
NGC 6791	An et al. (2009)	Carney et al. (2005)	

and are therefore not listed in Table 2. Data sources in italics are not yet reduced and not currently available for analysis.

Each of the cluster data sets in Table 2 has a different level of completeness, which will dictate which analysis projects the cluster can be included in. Clusters with complete photometry, although some may only have shallow 2MASS near-IR magnitudes, can have bulk binary population parameters determined, while complete deep photometry is necessary for the more detailed radial distribution analysis.

4.1. Optical Photometry

Many open clusters have been studied exhaustively using optical filters, including NGC 2099 and NGC 2682, and thus optical photometry for these clusters comes from previously published sources.

NGC 2099 optical photometry is pulled from Hartman et al. (2008), which used both short- and long-exposure images to provide *gri* magnitudes for $10 \leqslant r \leqslant 23$.

NGC 2682 falls within the Sloan Digital Sky Survey (SDSS; York et al. 2000) imaging region. The aperture photometry employed by SDSS caused problems for cluster photometry owing to crowding in cluster core regions. An et al. (2009) reanalyzed the *ugriz* SDSS images, extracting magnitudes using point-spread function (PSF) photometry, which can handle the dense cluster cores. Photometry in An et al. (2009) only covers two SDSS imaging regions near the core of NGC 2682 but does not touch regions farther out. In these sparse outer regions, the original SDSS data release 7 (DR7; Abazajian et al. 2009) aperture photometry is accurate enough to be used.

Due to the length of exposure (54 s) and telescope size (2.5 m), stars in the SDSS images begin to saturate above $r \sim 13$. Unfortunately, this removes almost all stars above the turnoff in NGC 2682. To fill in brighter stars that are not included in the SDSS catalog, *BVI* photometry from Yadav et al. (2008) is used as a supplement. The combination of these two photometry sources provides nearly complete coverage of the cluster in the optical, from $V \sim 10$ to $g \sim 23$.

4.1.1. MOSAIC

The MOSAIC instrument (Sawyer et al. 2010), outfitted with *UBVRI* filters, contains an array of eight 2048 × 4096 pixel CCD chips to create a single 8192 × 8192 pixel image. While it has been attached previously to the 4 m telescope at Kitt Peak National Observatory (KPNO), the data used in this project are from the WIYN 0.9 m telescope at KPNO. With roughly a square degree field of view, the MOSAIC images will allow us to analyze the entire spatial extent of any cluster observed.

Images of several open clusters were obtained with MOSAIC over several nights in 2000 February (Sarajedini & Kinemuchi, private communication). *UBVI* photometry was obtained on three clusters in the same set: M35, M36, and M37. For all clusters, both short and long sequences of images were taken. Short images had exposure lengths of 25, 8, 5, and 5 s in *UBVI*, respectively. Four images of the same exposure length were taken in each filter. Long-sequence images, also four per filter, had 10 times the exposure length of the short set: 250, 80, 50, and 50 s. Using both sequences together allows for photometry of the brightest and faintest stars within the cluster.

Two of the clusters have already been analyzed here: NGC 2168 in Thompson et al. (2014) and NGC 1960. For our

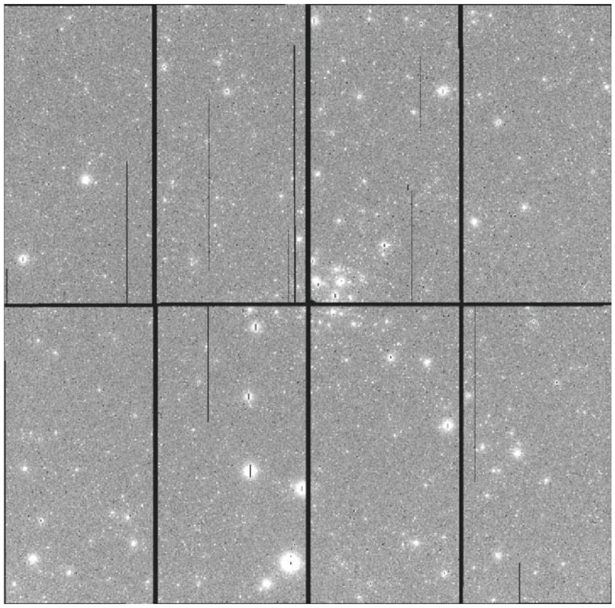

Figure 3. Reduced MOSAIC 50 s I-band image for NGC 1960.

analysis, the four images in each filter were combined to form a higher signal-to-noise ratio master image and to provide a complete covering of the cluster. Note the wide gap between chips in the individual MOSAIC images, shown in Figure 3. Each of the four images per filter was *dithered* (slightly offset) such that the combined image had no gaps in coverage.

These master images were then split into the eight individual chips on the MOSAIC image. This splitting was done to accommodate the DAOPHOT PSF photometry package, which has limits on image size. The individual 2k × 4k chips were the largest DAOPHOT could handle. In each chip (and for each master image), the process was the same. First, 400 candidate template stars were chosen to create a PSF. Next, the trimming process described in Thompson et al. (2014) was run, trimming the candidate list down to 250–300 template stars. Using this cleaned list, PSF parameters were determined and then applied through ALLSTAR.

Photometric quality plots for the short and long sets are shown in Figure 4. For reference, high-quality photometry has uncertainties less than 0.05. The MOSAIC images provide these high-quality data for $11 \leqslant V \leqslant 20$, covering nearly all of the stars within these clusters.

The ALLSTAR-derived magnitudes must be transformed to a standard system, in order to be comparable to other results. For calibration, photometry from the individual chips was recombined to produce single photometry files for each master image and then matched to previously published "standard" photometry. For NGC 1960, the previously published *UBVI* photometry from Sharma et al. (2006) was used to transform the instrumental MOSAIC magnitudes to the standard system.

Sources detected in the MOSAIC images were matched to the published photometry for each cluster, producing between 500 and 600 matches for each filter. Using these common stars, the instrumental ALLSTAR magnitudes were transformed via the following equations:

$$u = U + a_U + b_U \times (U - B) \tag{2}$$

$$b = B + a_B + b_B \times (B - V) \tag{3}$$

$$v = V + a_V + b_V \times (B - V) \tag{4}$$

Table 3
Transformation Coefficients for MOSAIC Photometry

Cluster	Filter	Length	a	b
NGC 1960	U	Short	1.843 ± 0.009	0.008 ± 0.011
		Long	-0.650 ± 0.010	-0.053 ± 0.008
	B	Short	1.191 ± 0.004	-0.105 ± 0.005
		Long	-1.305 ± 0.005	-0.127 ± 0.006
	V	Short	1.536 ± 0.003	0.048 ± 0.004
		Long	-0.928 ± 0.005	0.034 ± 0.006
	I	Short	1.993 ± 0.004	0.002 ± 0.004
		Long	-0.562 ± 0.011	-0.000 ± 0.011

$$i = I + a_I + b_I \times (V - I). \tag{5}$$

Here lowercase filter letters indicate instrumental (ALLSTAR-derived) magnitudes, while uppercase filters are those of the standard photometry. The transformation coefficients for each cluster and filter are located in Table 3. Transformations were done separately for the short- and long-exposure sequences. Residuals for these transformations are shown in Figure 5. Once the instrumental magnitude was calibrated to the standard system, all photometry was combined into a single master catalog.

4.2. JHK_S *Near-IR Photometry*

While 2MASS (Skrutskie et al. 2006) JHK_S photometry is available for all open clusters, it is too shallow ($J \sim 16$) to provide photometry for low-mass members of the cluster. New JHK_S near-IR photometry was obtained, by us, using the NEWFIRM instrument (Hoffman et al. 2004) on the Kitt Peak 4 m telescope. Images were taken on two nights in 2008 February. Observation and reduction processes are the same as used in Thompson et al. (2014), from which we published the NGC 2168 data.

Observations were taken in "4Q" mode, which offsets the telescope in a pattern to align the center of the cluster on each of the four NEWFIRM detectors. This allows for larger-area coverage than a single NEWFIRM field of view. To minimize errors in flat-fielding and negate cosmetic defects within the chips, the telescope was dithered between exposures for both clusters. Clusters have effective exposure times of 2400 s in J and H, and a total of 3600 s in K_S.

All images were reduced (dark correction, flat-fielding, sky subtraction) through the NEWFIRM pipeline (Swaters et al. 2009). The reduced images were stacked into master frames for each filter. Photometry was carried out using the DAOPHOT II and ALLSTAR programs (Stetson 1987), using a detection threshold of 3σ in all filters. Initially, 2000 stars were chosen to determine the PSF for each stacked image. This list was then trimmed to remove stars that degraded the fit. First, stars near bad or saturated pixels were removed, so as to avoid PSF distortion by these outliers. Next, stars that were less than 4 FWHM from another source were removed from the PSF list, ensuring that the PSF would not be contaminated by crowding. Finally, stars whose PSF χ^2 fit values were 2σ or more above the mean were removed. After trimming, approximately 500 and 800 stars remained for determining the PSF in NGC 2682 and NGC 2099, respectively.

The DAOPHOT-derived magnitudes were tied to the standard system by matching to 2MASS photometry. Only 2MASS sources with the highest photometric quality ("AAA") were used in the standard catalog. NGC 2682 frames matched

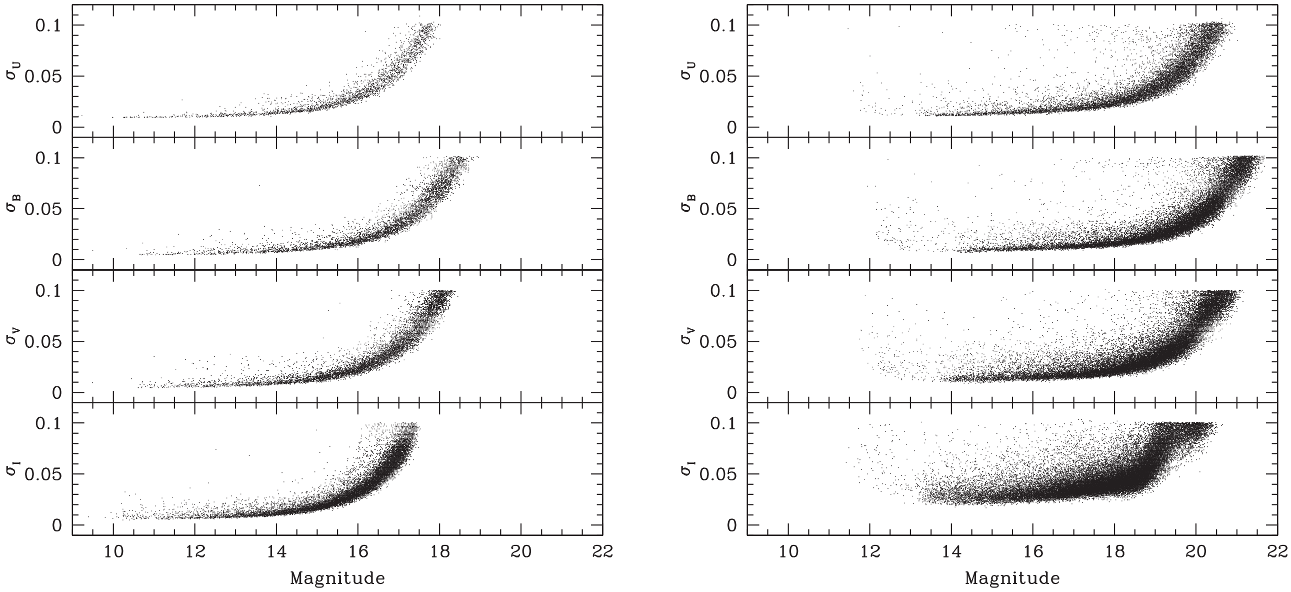

Figure 4. MOSAIC photometric quality plots for NGC 1960 in *UBVI*. Left: short set of exposures. Right: long set of exposures.

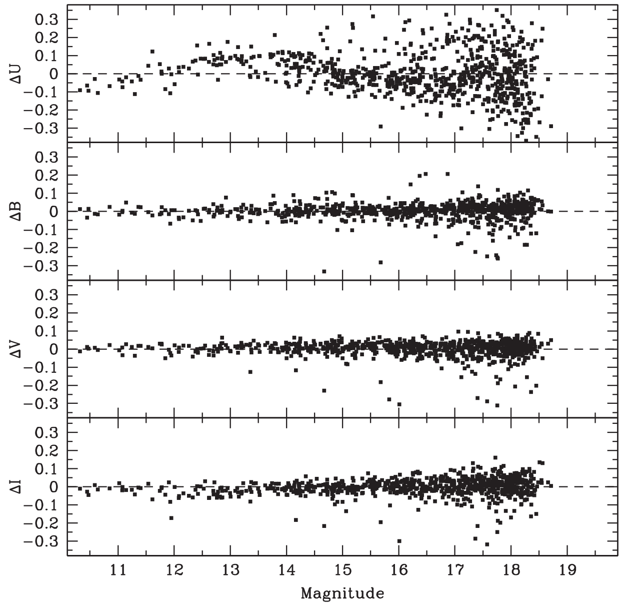

Figure 5. Residuals from transformation to standard system for NGC 1960 MOSAIC photometry.

approximately 700 stars between the NEWFIRM and 2MASS data sets, while NGC 2099 had almost 2000 overlapping sources. Using these matches, transformations were determined to the standard system for each cluster:

$$j = J + a_j(J - K_S) + b_j \tag{6}$$

$$h = H + a_h(H - K_S) + b_h \tag{7}$$

$$k = K_S + a_k(J - K_S) + b_k. \tag{8}$$

In Equations (6)–(8), lowercase letters denote DAOPHOT magnitudes, while uppercase letters denote 2MASS standard magnitudes. Transformation coefficients for each of the clusters is listed in Table 4.

A plot of transformation residuals is shown in Figure 6, along with measurement uncertainty as a function of magnitude. For almost all stars in the NEWFIRM images, magnitude uncertainties are < 0.1.

The NOAO/NEWFIRM photometry reaches a depth of approximately (J,H,K_S = 18.6, 18.1, 17.8).

4.3. Mid-IR Photometry

Deep mid-IR photometry ([3.6][4.5][5.8][8.0]) for NGC 2099 and NGC 2682 was gathered using the Infrared Array Camera (IRAC; Fazio et al. 2004) on the Spitzer Space Telescope. NGC 2682 data were obtained as part of cycle 2 proposal 20710 (PI Skrutskie), and NGC 2099 data were obtained from cycle 3 proposal 30800 (PI Frinchaboy). The data were taken in High Dynamic Range (HDR) mode, allowing measurement of the brightest and faintest stars in the cluster simultaneously. The data were reduced and photometered using the GLIMPSE (Galactic Legacy Infrared Mid-Plane Survey Extraordinare; Benjamin et al. 2003) pipeline, which was modified to handle the HDR data. The Spitzer/IRAC photometry reaches a depth of approximately ([3.6][4.5][5.8][8.0] = 18.0, 16.5, 14.6, 13.8). Although within this work, using the BINOCS method, we use only the [3.6] and [4.5] bands, for completeness purposes we provide this new photometry for all four Spitzer bands to the community in Table 5.

Supplemental mid-IR photometry (3–4.6 μm) is available from the Wide-field Infrared Survey Explorer (WISE; Wright et al. 2010) for the entire sky. WISE photometry was pulled for a 1° radius around the cluster, extending the spatial coverage of the mid-IR data. Unfortunately, WISE and IRAC use slightly different filters, and a correction must be applied to the WISE photometry in order to merge it with the deeper IRAC data.

WISE photometry and IRAC photometry of NGC 2099 were compared, and transformation equations were found using more than 800 common sources. Transformations were limited to $[3.4]_{\mathrm{WISE}} < 14$ and $[4.6]_{\mathrm{WISE}} < 13.5$, beyond which the transformations become problematic. Residuals between IRAC and WISE photometry show no correlation with color and only small magnitude offsets.

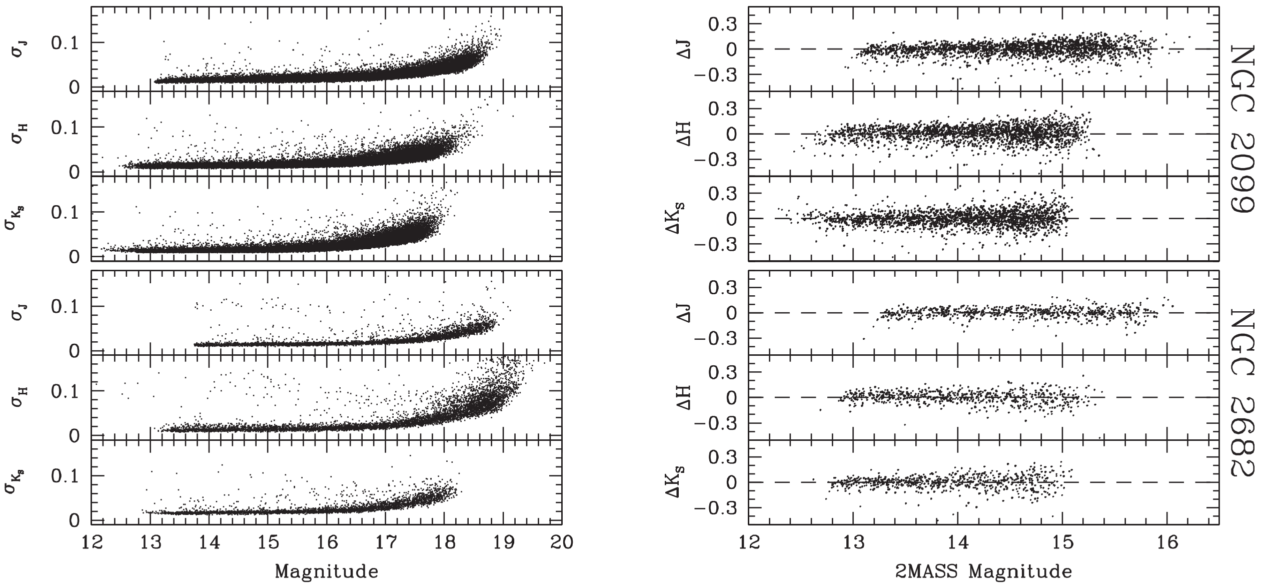

Figure 6. Left: NEWFIRM magnitude vs. uncertainty for NGC 2099 (top) and NGC 2682 (bottom). Right: transformation residuals between NEWFIRM magnitudes and 2MASS.

Table 4
NEWFIRM Transformation Coefficients

Cluster	J	H	K_S
NGC 1960	$a_j = -0.056 \pm 0.006$	$a_h = -0.177 \pm 0.018$	$a_k = +0.042 \pm 0.006$
	$b_j = +2.441 \pm 0.004$	$b_h = +2.620 \pm 0.003$	$b_k = +3.063 \pm 0.004$
NGC 2099	$a_j = -0.121 \pm 0.008$	$a_h = -0.354 \pm 0.016$	$a_k = +0.112 \pm 0.009$
	$b_j = +2.434 \pm 0.004$	$b_h = +2.318 \pm 0.003$	$b_k = +3.020 \pm 0.005$
NGC 2168	$a_j = -0.099 \pm 0.005$	$a_h = -0.296 \pm 0.012$	$a_k = +0.093 \pm 0.007$
	$b_j = +2.397 \pm 0.003$	$b_h = +2.297 \pm 0.002$	$b_k = +3.030 \pm 0.005$
NGC 2420	$a_j = -0.036 \pm 0.008$	$a_h = -0.234 \pm 0.020$	$a_k = +0.130 \pm 0.011$
	$b_j = +2.752 \pm 0.005$	$b_h = +2.739 \pm 0.003$	$b_k = +3.179 \pm 0.006$
NGC 2682	$a_j = -0.100 \pm 0.010$	$a_h = -0.250 \pm 0.021$	$a_k = +0.113 \pm 0.014$
	$b_j = +2.444 \pm 0.007$	$b_h = +2.277 \pm 0.004$	$b_k = +2.956 \pm 0.010$

$[3.4]_{\rm WISE}$ and $[3.6]_{\rm IRAC}$ are interchangeable in the specified region, while $[4.6]_{\rm WISE} = [4.5]_{\rm IRAC} + 0.03$. A plot of residuals for this transformation is shown in Figure 7. Using these simple transformation equations, WISE photometry was merged with the IRAC sources.

4.4. Merged Data Set

Optical, near-IR, and mid-IR photometry sets for each cluster are merged into a final data set. Final cluster CMDs and spatial distributions are shown in Figures 8 and 9.

The IRAC coverage area in NGC 2682 is only a thin stripe in decl., designed to overlap the 2MASS 6x calibration area. WISE photometry is necessary to implement the BINOCS detection method across the entire cluster area.

5. Stellar Isochrone Models

The BINOCS code uses synthetic SEDs from isochrones to determine best-fit masses for each star in the clusters. Therefore, the mass determination from the BINOCS code is only as accurate as the underlying isochrones themselves.

Modern stellar models are still affected by nonnegligible discrepancies due to variation in input physics (Valle et al. 2013). This is apparent in the comparison of isochrone tracks computed by different sets of authors. In Figure 10, two popular isochrone sets are overplotted on NGC 2682 and NGC 2099 CMDs: Dartmouth (Dotter et al. 2007) and Padova (Girardi et al. 2002) or PARSEC (Bressan et al. 2012). For NGC 2682, 3.5 Gyr isochrones with $[{\rm Fe/H}] = +0.01$, $E(B\text{–}V) = 0.04$, and a distance of 855 pc were used. For NGC 2099, 355 Myr isochrones were used, with $[{\rm Fe/H}] = +0.08$, $E(B\text{–}V) = 0.3$, and a distance of 1386 pc. Dartmouth isochrones can only be interpolated in [Fe/H] for ages >1 Gyr. Because no 355 Myr Dartmouth isochrones with $[{\rm Fe/H}] = +0.08$ can be generated, they are not shown in Figure 10.

It is clear from Figure 10 that all the isochrone sets deviate from the observed main sequence, especially for low-mass stars. To quantify the deviation between the models and

Table 5
New NEWFIRM and IRAC Photometry

Cluster (NGC) (1)	R.A. (2000.0) (2)	Decl. (2000.0) (3)	*J* (mag) (4)	*H* (mag) (5)	K_S (mag) (6)	[3.6] (mag) (7)	[4.5] (mag) (8)	[5.8] (mag) (9)	[8.0] (mag) (10)
2682	132.73465	11.77622	14.189 ± 0.011	13.613 ± 0.013	13.445 ± 0.016	13.410 ± 0.024	13.451 ± 0.069	13.415 ± 0.040	13.402 ± 0.083
2682	132.73955	11.58258	13.921 ± 0.011	13.410 ± 0.011	13.297 ± 0.017	13.208 ± 0.020	13.247 ± 0.056	13.181 ± 0.035	13.205 ± 0.067
2682	132.74037	12.01129	14.141 ± 0.012	13.702 ± 0.011	13.671 ± 0.022	13.557 ± 0.023	13.618 ± 0.051	13.536 ± 0.036	13.608 ± 0.076
2682	132.74144	12.08310	14.283 ± 0.012	13.744 ± 0.012	13.624 ± 0.021	13.566 ± 0.022	13.551 ± 0.055	13.488 ± 0.037	13.573 ± 0.070
2682	132.74359	11.80183	14.073 ± 0.011	13.635 ± 0.011	13.556 ± 0.015	13.486 ± 0.023	13.524 ± 0.059	13.489 ± 0.033	13.367 ± 0.065
2682	132.74379	11.81218	13.993 ± 0.011	13.571 ± 0.009	13.512 ± 0.014	13.438 ± 0.021	13.443 ± 0.039	13.416 ± 0.030	13.422 ± 0.068
2682	132.74596	11.80808	14.299 ± 0.011	13.778 ± 0.010	13.713 ± 0.017	13.586 ± 0.018	13.512 ± 0.045	13.536 ± 0.033	13.527 ± 0.057
2682	132.74651	11.97064	14.615 ± 0.014	13.908 ± 0.014	13.887 ± 0.025	13.670 ± 0.019	13.732 ± 0.053	13.689 ± 0.038	13.613 ± 0.068
2682	132.74748	12.16521	14.022 ± 0.016	13.567 ± 0.021	13.569 ± 0.035	13.283 ± 0.030	13.393 ± 0.044	13.362 ± 0.033	13.278 ± 0.053
2682	132.74765	11.91457	14.125 ± 0.015	13.673 ± 0.018	13.573 ± 0.024	13.480 ± 0.022	13.504 ± 0.039	13.451 ± 0.033	13.329 ± 0.053

Note. This table is available in its entirety in machine-readable form in the online journal. A portion is shown here for guidance regarding its form and content.

(This table is available in its entirety in machine-readable form.)

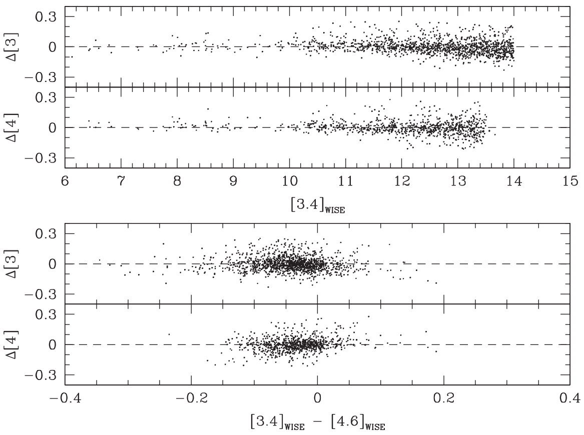

Figure 7. Residuals from transformation between WISE and IRAC magnitudes for sources near NGC 2099.

observations, residuals between a by-eye empirical ridgeline and isochrones in various filters are shown in Figure 11. The NGC 2682 *ugriz* empirical ridgelines are pulled from the same source as the data, An et al. (2009). For stars with magnitudes above or below the ridgeline area, colors are shifted such that the adjusted ridgeline is continuous.

Isochrone models vary anywhere from ∼0.1 to over 0.3 in color, depending on filter. This large discrepancy in color may significantly affect results from the BINOCS fitting. Before being used to compute synthetic SEDs, these isochrones will have to be altered.

To correct the isochrones so that they more closely match the data, isochrones are adjusted to align with the hand-drawn ridgelines. This is done by assuming that the bolometric correction to the *r* filter (and hence the *r* magnitude itself) is correct and adjusting all colors accordingly to match the empirical ridgelines. This updated isochrone is then fed into the BINOCS code to create synthetic SEDs.

For all BINOCS runs, PARSEC isochrones were used. While the PARSEC isochrones showed the most deviation from the empirical ridgelines in Figure 11, this error is corrected out by the empirical transformation. Of the isochrone sets considered, PARSEC provides the largest mass range of synthetic stars and is therefore the most advantageous for this approach.

6. BINOCS Testing

When the BINOCS code was introduced in Section 2.3, several parameters were assumed: the number of iterations of the fitting, the number of "good" fitting filters, and the threshold to consider a magnitude "good." Each of these parameters was tested, and the results are shown below.

6.1. Number of Iterations

The BINOCS fitting is iterated a number of times to produce best-fit masses and uncertainties. While the BINOCS code has random elements (sampling of Gaussian error distribution), if the process is iterated enough times, the final results will not vary greatly. Running excess iterations beyond this will use more computing time but not enhance the results in any meaningful way. To determine the minimum number of iterations required, the combined NGC 2682 data set was run through the BINOCS code with varying numbers of iterations: 3, 10, 30, 90, 150, 200, 300, 400, 500, 600, 700, 1200.

For each number of iterations, the BINOCS code was run five times. Using these five runs, a "% uncertainty," Σ, was computed for each star. Σ is defined as the standard deviation of all five resulting masses divided by the average of the resulting masses for which the star is classified as a member. Σ for primary and secondary mass determinations are computed independently. Stars that were classified as nonmember stars in all five runs (and hence not given any best-fit masses) were removed from the set.

After computing Σ for all stars in the NGC 2682 data set, median and 95th percentile Σ were computed for each iteration value. The results are shown in Figure 12.

Median Σ values are overall quite low; both primary and secondary median Σ are equal to zero for any number of iterations $\geqslant 150$. In order to ensure that a majority of stellar-mass determinations are roughly constant between runs, we require the 95th percentile Σ to be less than 0.1: on average, there will be a less than 10% difference in derived stellar masses between runs for 95% of stars in the data set. Using 300 iterations of the BINOCS fitting will satisfy this requirement (as seen in Figure 12), and this is chosen as the ideal number of iterations in the final computations.

6.2. Number of Good Filters

While a comprehensive sampling of the SED over all 10 filters (*UBVRI* or *ugriz*, JHK_S, [3.6][4.5]) is ideal, it is often impractical to obtain quality photometry in this number of bands for every cluster we wish to study. In practice, the BINOCS code will have to produce accurate results using a less-than-ideal number of filters.

The library of synthetic SED models generated from the best-fit isochrone for NGC 2682 ($[\mathrm{Fe/H}] = +0.01$, age = 3.55 Gyr) was used as an input into the BINOCS code. Using the combined NGC 2682 data set, average photometric uncertainties were computed for all bands in bins of 0.5 mag. Every magnitude in the input library was randomized using a Gaussian with $\sigma = 2\times$ the average photometric uncertainty in the corresponding bin.

The BINOCS code was run on the input library for various combinations of usable filters. For each run, only certain filter magnitudes in the randomized library were transferred to the final input file, listed in the first column of Table 6.

Each filter combination was run five times, and each time the % error in the primary- and secondary-mass determination was recorded. After all five runs, stars were binned into steps of 0.1 in mass ratio, and average % error + 1 standard deviation was computed for all stars in the bin. This 1σ % error is shown for each bin and filter combination in Table 6.

The "332" (*griJHK*$_S$[3.6][4.5]) filter combination is chosen as the preferred option for this work. Only requiring three optical filters increases the number of usable clusters while only marginally increasing the uncertainty in the final BINOCS results. For primary-mass estimates the "332" combination produces the second-lowest 1σ % errors of all scenarios and produces secondary-mass estimates good to within 20%. The only better scenario is the full photometry set (532), which is difficult to obtain for many open clusters, especially depth in the *u* filter.

Using these results, there are 1500 stars in NGC 2682 and 3500 stars in NGC 2099 that have the necessary number of filters for a good BINOCS fitting.

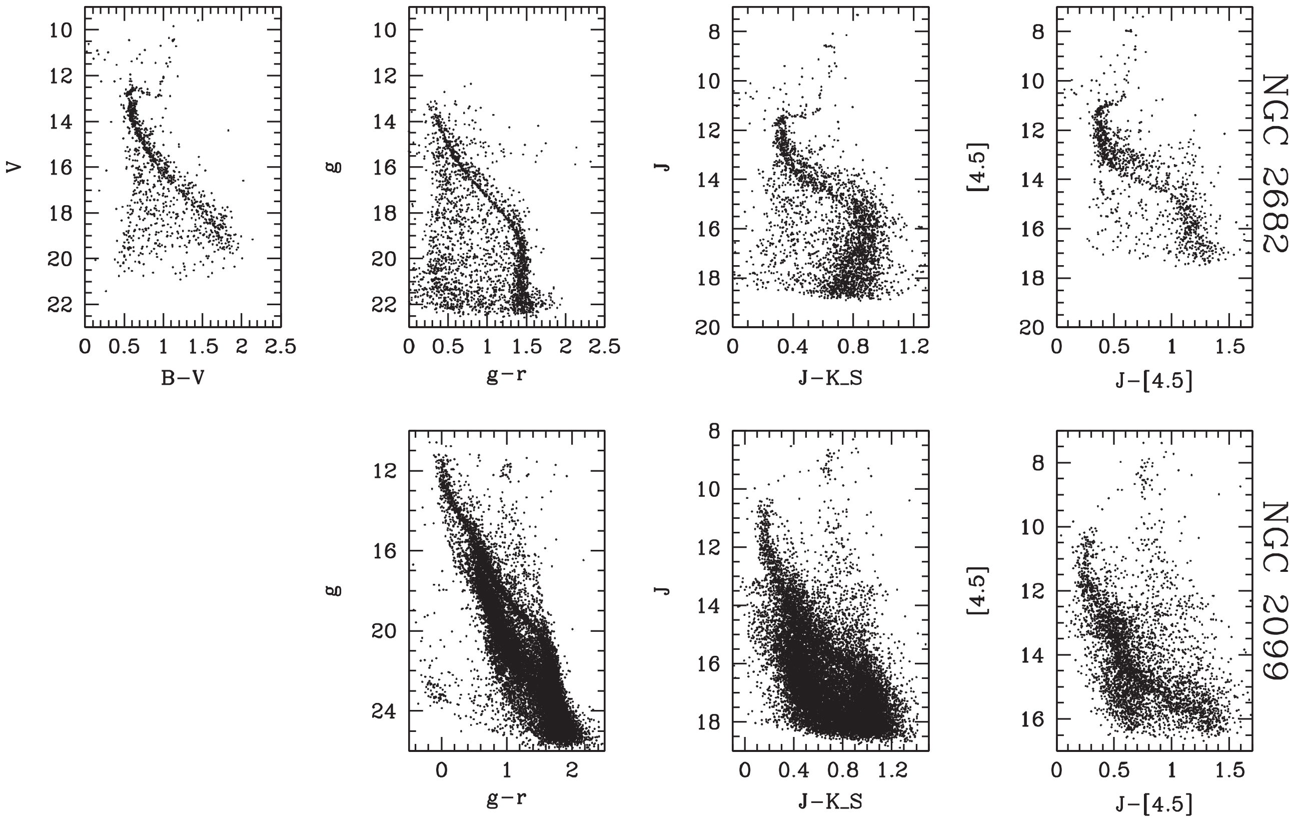

Figure 8. Cluster CMDs for merged data sets. NGC 2682 includes supplementary *BVI* photometry to include stars above the turnoff. CMDs are shown only for sources within 20′ of the cluster centers.

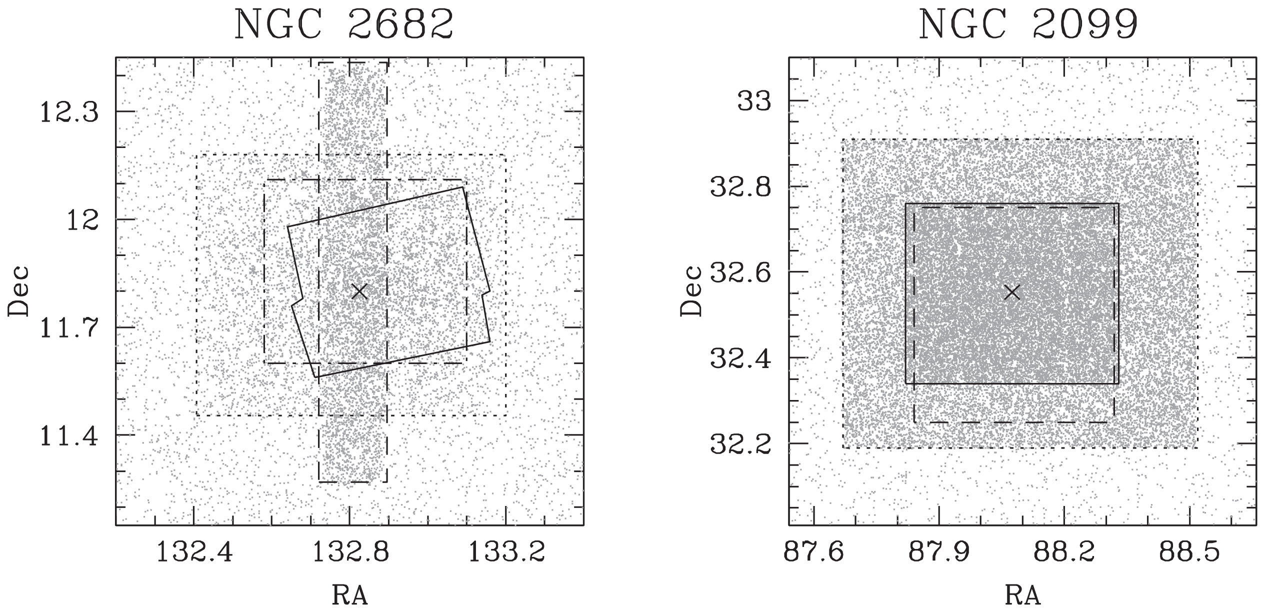

Figure 9. Cluster spatial diagrams for merged data sets. Solid lines show *gri* photometry data sets: Hartman et al. (2008) for NGC 2099, An et al. (2009) for NGC 2682. Dotted lines show NEWFIRM JHK_S photometry. Dashed lines show IRAC mid-IR photometry. Dotted–dashed lines show supplemental *BVI* photometry from Yadav et al. (2008) for NGC 2682. 2MASS near-IR and WISE mid-IR photometry is available for all sky. NGC 2682 SDSS DR7 photometry is available over the entire plotted area.

6.3. “Close” Filter Threshold

In addition to generating accurate mass estimates for cluster stars, the BINOCS method can mark stars as nonmembers if they do not have the required number of “close” filters. Therefore, the threshold ($\frac{1}{|\, m_{\mathrm{star}} - m_{\mathrm{model}} \,| + \eta_{\mathrm{soft}}} < X$) that defines whether a filter is “close” will adjust the level of field star contamination within the sample. Conversely, if the threshold is too stringent, many legitimate member stars may be discarded from the sample.

To test for the optimal threshold level, an input catalog was created similarly to that used in Section 6.2. The input file to

Table 6
1σ% Errors in Mass Estimates for Various Combinations of Filters

	Mass Ratio											
Filters	0.0	0.1	0.2	0.3	0.4	0.5	0.6	0.7	0.8	0.9	1.0	
101: .*g*[3.6].	6.6	0.0	0.1	1.1	1.2	2.5	4.1	4.9	5.1	6.2	9.6	-901σ % Error in M_{pri}
111: .*g*...*J*..[3.6].	6.0	0.0	0.1	0.9	1.0	1.8	3.1	3.7	3.9	4.7	9.1	
202: .*gr*.....[3.6][4.5]	2.3	0.0	0.0	0.7	0.8	1.5	3.3	3.6	3.7	4.5	7.6	
211: .*gr*..*J*..[3.6].	2.7	0.0	0.0	0.7	0.7	1.8	3.0	3.6	3.8	4.5	7.9	
212: .*gr*..*J*..[3.6][4.5]	2.5	0.0	0.0	0.7	0.7	1.3	2.9	3.4	3.4	4.1	7.7	
222: .*gr*..*J*.K_S[3.6][4.5]	2.6	0.0	0.0	0.6	0.7	1.2	2.2	3.0	3.3	3.9	6.9	
322: .*gri*.*J*.K_S[3.6][4.5]	1.5	0.0	0.0	0.6	0.7	0.9	1.9	2.4	2.7	3.3	6.1	
332: .*gri*.*JH*K_S[3.6][4.5]	1.4	0.0	0.0	0.5	0.6	0.9	1.9	2.5	2.8	3.3	6.2	
532: *ugrizJH*K_S[3.6][4.5]	0.6	0.0	0.0	0.2	0.2	0.5	0.8	1.4	1.8	1.9	4.4	
101: .*g*......[3.6].	...	0.0	66.5	37.3	26.1	18.7	17.1	17.3	14.5	12.1	13.0	-901σ % Error in M_{sec}
111: .*g*...*J*..[3.6].	...	0.0	43.7	29.4	20.7	16.1	11.3	10.4	9.9	8.8	11.2	
202: .*gr*.....[3.6][4.5]	...	0.0	51.6	24.4	15.7	11.9	10.5	9.0	7.5	7.2	10.0	
211: .*gr*..*J*..[3.6].	...	0.0	39.9	32.8	18.5	12.6	9.7	10.5	8.0	7.3	10.3	
212: .*gr*..*J*..[3.6][4.5]	...	0.0	44.9	23.5	15.8	11.4	8.9	8.3	6.9	6.4	10.1	
222: .*gr*..*J*.K_S[3.6][4.5]	...	0.0	27.6	16.6	13.4	9.1	7.2	7.3	6.5	6.2	8.6	
322: .*gri*.*J*.K_S[3.6][4.5]	...	0.0	38.1	18.8	11.1	7.1	5.7	5.8	5.0	4.8	7.7	
332: .*gri*.*JH*K_S[3.6][4.5]	...	0.0	19.7	15.0	10.6	8.3	5.5	5.6	5.3	4.8	7.8	
532: *ugrizJH*K_S[3.6][4.5]	...	0.0	37.7	13.5	10.4	6.0	3.3	3.8	3.7	2.9	5.3	

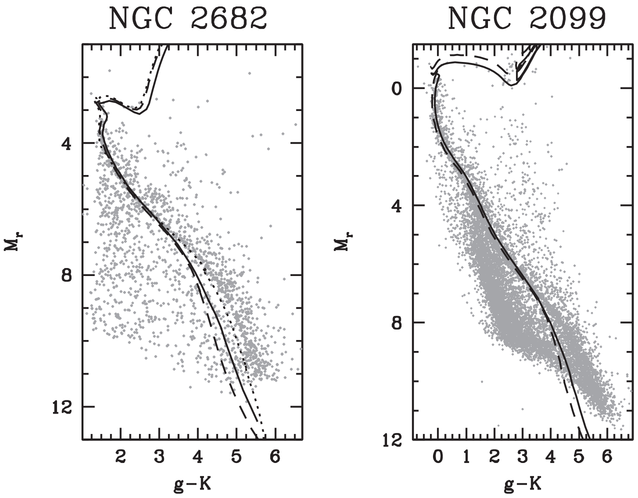

Figure 10. Comparison of popular isochrone sets to combined cluster photometry in several CMDs. Dotted line: Dartmouth (Dotter et al. 2007; NGC 2682 only). Solid line: Padova (Girardi et al. 2002). Dashed line: PARSEC (Bressan et al. 2012). NGC 2682 isochrones: 3.5 Gyr, [Fe/H] = +0.01, $E(B–V) = 0.04$, 1386 pc. NGC 2099 isochrones: 355 Myr, [Fe/H] = +0.08, $E(B–V) = 0.3$, 1386 pc.

the BINOCS code contained three copies of the synthetic library created in Section 6.2: one at the same distance as NGC 2682, one shifted a distance modulus of 0.8 nearer, and one shifted a distance modulus of 0.8 farther than NGC 2682. As the magnitude difference between the single-star main sequence and equal-mass binary sequence is 0.753, there should be no degeneracies between the three copies of the input library.

The BINOCS code was run on the input file for various values of the threshold. After the run was complete, two numbers were computed: the percentage of member stars (from the copy of the library at NGC 2682's distance) that were classified as nonmembers, and the percentage of nonmember stars (from the other two copies of the library) that were classified as members. The best-fit "close" threshold value is chosen such that the sum of these two values is at a minimum.

Figure 13 shows the results of the threshold testing. A minimum in % Total is found at a threshold value of 10. Contamination from foreground and background stars quickly increases when threshold values are larger than 10, while the percentage of missed member stars only decreases gradually.

A formal χ^2 form of Equation (1) was also explored in addition to the fixed-width threshold form used:

$$\Theta = \sum_{\mathrm{filters}} \frac{(m_{\mathrm{star}} - m_{\mathrm{model}})^2}{\sigma_{\mathrm{star}}^2}. \tag{9}$$

While the χ^2 form produced less theoretical contamination in this test, it also classified *more than 90% of the stars in the NGC 2682 data set as nonmembers!* As this is unrealistic for a cluster so far from the Galactic plane, the fixed-width threshold form of Equation (1) was used in the final BINOCS code.

6.4. Minimum Mass Ratio

It is often impossible to tell the difference between a single star and a low mass ratio binary, even when using a minimum of eight filters. A minimum mass ratio, as a function of primary mass, is determined to be the maximum of three values:

1. *Lowest mass ratio model:* For the PARSEC isochrones being used, the lowest-mass model has a mass of 0.13 $M_\odot$, defining a minimum model mass ratio for each primary mass.
2. *Synthetic best-fit mass ratio:* After each run of the BINOCS code, a test similar to that in Section 6.2 is run. Minimum mass ratios are defined as the resulting best fit of each synthetic single star.
3. *Constant threshold:* After a detailed comparison to clusters that have RV comparisons available, we find that BINOCS results prove unreliable, single/binary indistinguishable, for stars with $q < 0.3$ (see Section 7). Even if the synthetic tests estimate a value less than this, the minimum threshold for identifying a binary is a mass ratio $q \geqslant 0.3$.

Stars are defined to be singles if they have best-fit mass ratios below the specified value. Minimum mass ratios for

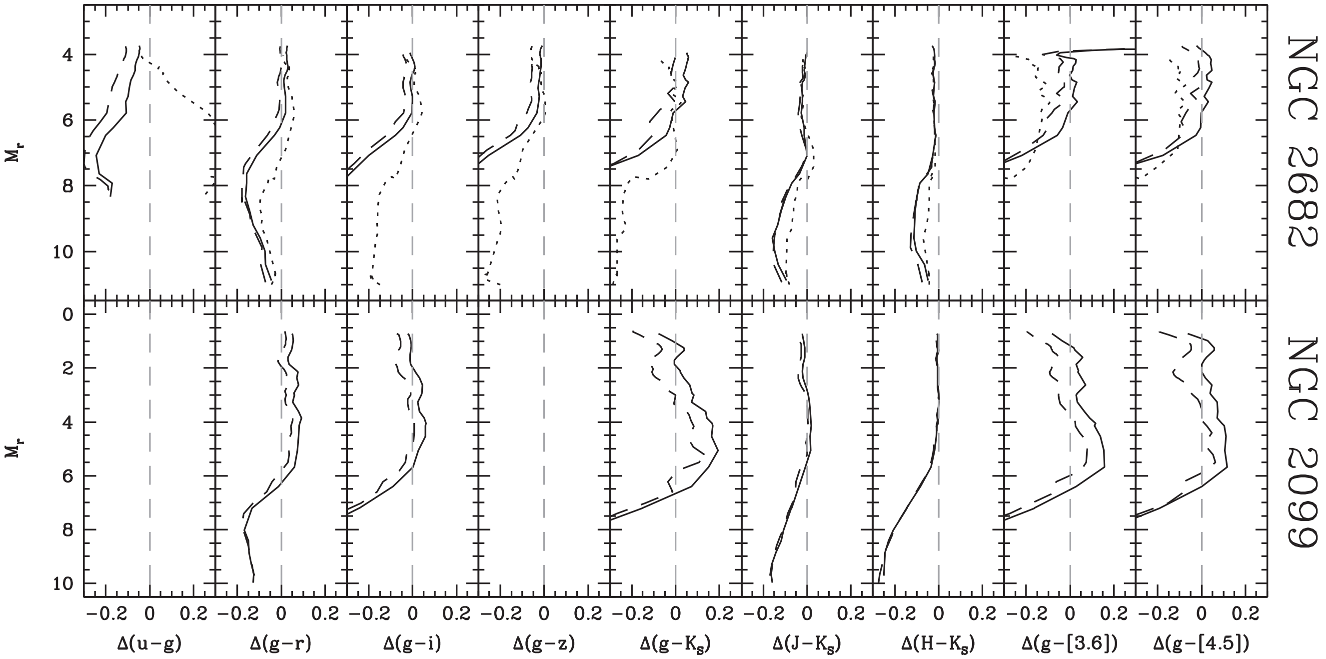

Figure 11. Residuals between empirical ridgelines and isochrones for various filters. Same isochrones as shown in Figure 10. Dotted line: Dartmouth (Dotter et al. 2007). Solid line: Padova (Girardi et al. 2002). Dashed line: PARSEC (Bressan et al. 2012).

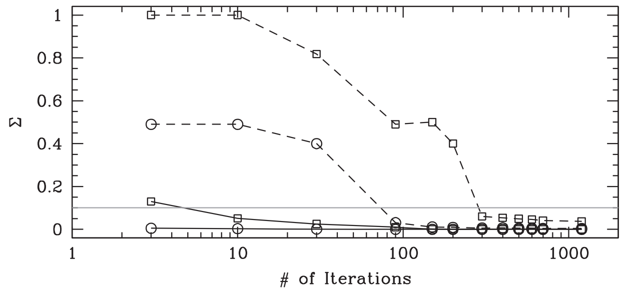

Figure 12. Results of the number of iterations test. Circles correspond to Σ for primary masses, while squares correspond to secondary-mass Σ. Solid lines show median Σ; dashed lines show 95th percentile. The gray line denotes the average 10% uncertainty between runs.

NGC 2099 are shown in Figure 14. For systems with primary masses below $0.5\,M_\odot$, minimum mass ratios are dominated by the minimum model mass of $0.13\,M_\odot$. Above a primary mass of $2.5\,M_\odot$, minimum mass ratios are dominated by degeneracies at the turnoff. As shown in Figure 14, the BINOCS technique works well between 2.5 and $0.5\,M_\odot$ for NGC 2099.

In their analysis, de Grijs et al. stated that their analysis was only sensitive to binaries with $q \geqslant 0.55$. The BINOCS method shows an improvement in mass sensitivity, with minimum mass ratios closer to 0.35 for a large mass range.

7. Results

The BINOCS results for NGC 2682 were compared to a published RV study of 104 cluster members (26 binaries) by Mathieu & Latham (1986). A comparison of multiplicity determinations is shown in Table 7 and Figure 15. The comparison was limited to stars with $14.5 \leqslant g \leqslant 16.5$, avoiding the degeneracies at the turnoff and ending at the lower magnitude limit for the RV study.

Using the updated minimum mass ratio calculation in Section 6.4, there is good agreement between BINOCS and RV results, with 60% of RV singles being confirmed as single stars by the BINOCS routine, and 56% of RV binaries being confirmed.

Each method has its own limitations and biases, and exact agreement is not expected. RV surveys cannot detect long-period binaries, or those with high inclination, while BINOCS is insensitive to these parameters. These types of systems may account for many of the 29 RV-single stars that the BINOCS routine fit as binaries. The four RV-binary stars that BINOCS determined to be singles may be systems with small secondaries. RV shifts for small companions may still be appreciable, while the amount of contributed light to the SED is not. The RV and BINOCS methods are complementary techniques but still show a large amount of overlap in the results. Unfortunately, neither NGC 2682 nor NGC 2099 has published double-line spectroscopic binaries with masses determined.

The BINOCS results for NGC 2168 were compared to a published RV study of the cluster in Geller et al. (2010). A comparison of multiplicity determinations is shown in Table 8 and Figure 16. To avoid complications from the turnoff and poor faint data in the RV studies, the comparison is limited to a specific magnitude range. For NGC 2168, only stars with $14.2 \leqslant V \leqslant 16.5$ are considered.

Of stars classified as binaries by BINOCS, many are also classified as binaries by RV detection methods, with a 69% overlap in NGC 2168. The BINOCS code shows a lower match when classifying RV singles,[6] with only 59% of RV singles being classified as singles by BINOCS in NGC 2168. To ensure reasonable agreement between BINOCS and Geller et al. (2010), a floor of 0.3 was set in the minimum mass ratio calculation.

Using the updated minimum mass ratio calculation in Section 6.4, there is good agreement between BINOCS and RV results, with 60% of RV singles being confirmed as single stars by the BINOCS routine, and 56% of RV binaries being confirmed.

---

[6] The term “RV singles” is used to denote a system that does not show an appreciable velocity shift.

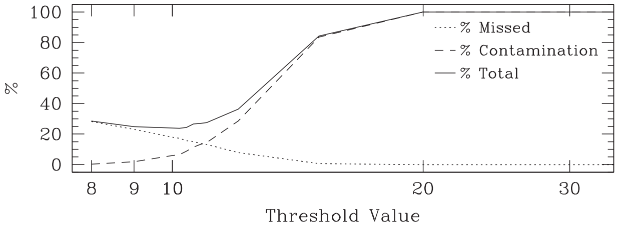

Figure 13. Results of the threshold test for NGC 2682. Best threshold chosen to minimize % Total.

7.1. Mass Determination

While not a part of the analysis set owing to the lack of deep near-IR photometry, the clusters NGC 188 and NGC 6819 have also been the subject of detailed RV studies (Geller et al. 2008; Hole et al. 2009, respectively). A comparison to the RV studies can be completed in the region where 2MASS photometry is available .

Of the 1046 stars studied in NGC 188, 13 were *double-lined* binaries. Further follow-up on these stars, published in Geller et al. (2009), characterized the orbits of these double-lined binaries and produced accurate binary mass ratios. Similarly, NGC 6819 stars were followed up in Milliman et al. (2014), and 15 double-lined binaries were detected. The RV-determined mass ratios are compared to those from BINOCS in Figures 17 and 18.

There are several highly discrepant mass ratio determinations in NGC 188 and NGC 6819. Many of these double-lined systems lie near the turnoff of each cluster, where the single-star main sequence and equal-mass binary sequence overlap (as seen in the left panel of Figure 17). In these regions, there are natural degeneracies, and the BINOCS code cannot accurately determine parameters. Stars marked by red circles in Figure 17 lie extremely close to these degeneracies and therefore exhibit large errors with respect to the RV results.

Ignoring those stars very close to the crossing of single-star main sequence and equal-mass binary sequence, there is close agreement between RV and BINOCS mass ratios. Including the quoted uncertainties in mass from BINOCS (uncertainties from the RV surveys are negligible), mass ratios largely agree to within 10%.

Combining this 10% mass ratio accuracy with the previous conclusion that BINOCS results are largely agreeing with RV multiplicity determinations, it is clear that the BINOCS code is producing accurate results that can be extrapolated to lower-mass stars.

7.2. Membership Comparison to Gaia

One additional effect of the BINOCS analysis is that stars are classified as single or binary members and nonmembers. The ability to reject SEDs that cannot fit for stars of the correct distance, reddening, and luminosity class can be a powerful tool for exploring faint membership and binarity of simple populations.

To test the effectiveness to photometric "cleaning" of nonmember stars from the cluster CMD for main-sequence stars, we have made a comparison to the Gaia DR2 (Gaia Collaboration et al. 2016, 2018) proper-motion-based membership probability using the method from Donor et al. (2018) for two of our clusters, NGC 2099 and NGC 2682. While the BINOCS method will not be as effective as Gaia, the simplicity of using only photometry allows probing much deeper than Gaia.

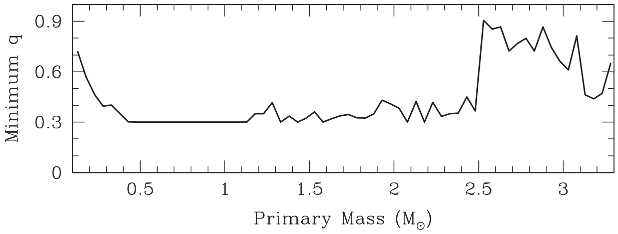

Figure 14. Minimum mass ratios for NGC 2099, as a function of primary mass.

Table 7
Comparison of BINOCS and Mathieu & Latham (1986) RV Multiplicity Results for NGC 2682 (as Shown in Figure 15)

	BINOCS		
	Single	Binary	Nonmember
RV-single	81	29	25
RV-binary	4	24	15

We cross-matched the Gaia to the BINOCS analyzed stars, where we then compared two methods to see how reliable they are in identifying cluster members: (1) the BINOCS membership method, and (2) the Gaia proper-motion-based membership method. We found for the cluster NGC 2682 (Figure 19 and Table 9) that for stars fainter than $H \sim 12$, main-sequence stars, the BINOCS method agrees fairly well with Gaia, with BINOCS finding members for ~86% of the Gaia members with significant overlap in members along the main sequence, which cuts off at magnitudes $H \sim 16$ owing to the limit of Gaia photometry and proper motions. However, we do find that the BINOCS method is not quite as discriminating, as it finds 543 members compared to 414 with Gaia.

We performed the same comparison for the cluster NGC 2099 (Figure 20 and Table 9). The BINOCS method members again overlap with many of the Gaia members in the main-sequence portion of the CMD and cuts off at magnitudes around 16, due to the same limitations. In this plot, far more stars in the BINOCS sample are considered to be members of NGC 2099, as compared to NGC 2682, since this younger cluster has a longer main sequence where BINOCS works well. For this cluster, BINOCS categorizes ~92% of the Gaia members correctly as members, but again it includes more Gaia nonmember stars as members.

As a comparison to Gaia proper-motion membership, one of the best membership methods available, we find that BINOCS agrees with Gaia membership >75% of the time on the main sequence but is more inclusive on nonmembers. However, BINOCS can be used at large distances, unlike Gaia, such as to explore membership and binarity in simple stellar populations in other galaxies, given sufficient photometric depth (e.g., Hubble + JWST).

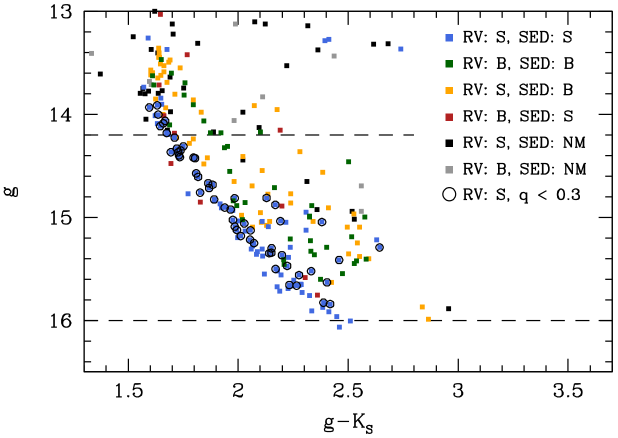

Figure 15. CMD comparison of RV and BINOCS SED-fitting results for NGC 2682. Stars considered in comparison are those within dashed line limits. Colors indicate which cell of Table 7 the star belongs to. Black circles indicate RV singles that were classified as BINOCS best-fit binaries with mass ratios < 0.3.

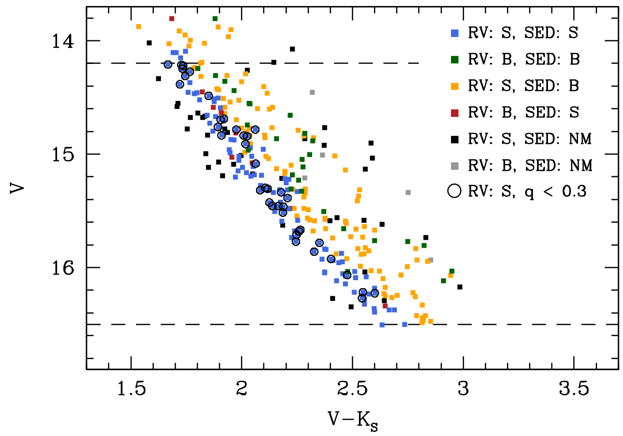

Figure 16. CMD comparison of RV and BINOCS SED-fitting results for NGC 2168. Stars considered in comparison are those within dashed line limits. Colors indicate which cell of Table 8 the star belongs to. Black circles indicate RV singles that were classified as BINOCS best-fit binaries with mass ratios < 0.3.

7.3. Binary Fractions

After validating the BINOCS code, it can begin to be applied to the clusters in the analysis set with the requisite photometry. The BINOCS code was run on each of the eight clusters available for this analysis (see Table 1), and the overall binary fraction was recorded. A list of clusters, their parameters, and the associated overall binary percentage is shown in Table 10.

7.3.1. Binary Fraction versus Age

One of the main science questions of this work is how the binary population of a cluster evolves over time. The trend of overall binary fraction with cluster age is shown in Figure 21. Overall, there seems to be a decreasing trend with age. Gravitational interactions between stars can easily disrupt some binary systems, while creating binaries from two single stars is much less common. It appears that the majority of binary disruption occurs quickly during the first 200 Myr of a cluster's lifetime, after which the binary fraction becomes fairly constant.

After about 200 Myr, the binary fraction stabilizes to around 0.42, which is slightly higher than the measured binary percentage of 0.33 for field stars (Raghavan & McAlister 2009). This small difference may be attributable to the fact that during the strong gravitational interaction that could eject a cluster binary system into the field population, the binary system may also be disrupted. Without a better understanding of the ejection processes of binary systems, the overall binary fraction of cluster and field stars cannot be easily compared.

Completing an analysis such as the one in Figure 21 using only RV surveys could take decades to build up enough analysis clusters to produce any useful insights. Two-band analysis, though fast, is dominated by degeneracies and is limited to small magnitude ranges across the main sequence. With new, deep photometric surveys becoming available (UKIDSS, VVV, ESA Gaia, LSST), more clusters could be added to the list with minimal effort using the BINOCS code. Generating the plot in Figure 21 using hundreds of open clusters would yield significant insights into the true distribution of binary fractions.

7.3.2. Binary Fraction versus Metallicity

It is not well understood how differences in metallicity of a pre-cluster cloud may affect the formation of binary systems. The distribution of binary fractions as a function of metallicity is shown in Figure 21. There are only seven clusters shown in Figure 21 owing to the fact that M36 does not have a published metallicity value.

It is clear from Figure 21 that any observed trend will be dominated by the contribution from NGC 6791, at [Fe/H] = +0.38. Without this metallicity outlier, there is hardly any trend in binary fraction. The absence of a trend is still significant: the metallicity of a primordial cluster may have no effect on the binary population, at least on the aggregate level. This insight could be important for initial conditions of numerical simulations.

Similarly to the distribution with age, more data points can be added to this plot with minimal effort when new deep photometry becomes available. Filling in the remainder of the metallicity range will give more insight into whether a trend exists or not. Additionally, with a much larger number of clusters, binary fraction can be modeled as a function of both metallicity *and* age.

7.3.3. Binary Fraction versus Galactocentric Radius

The above two comparisons have linked binary fraction to intrinsic cluster parameters, but clusters are not isolated systems, and the galactic environment plays a large part in cluster evolution. Clusters that are born near the center of the Galaxy experience a higher rate of tidal stripping events and other interactions which may alter the binary population. Figure 21 shows the overall binary fraction of clusters as a function of galactocentric radius (R_{gc}; the distance the cluster is from the center of the galaxy).

In Figure 21, any observed trend is dominated by the two very young clusters, and thus high binary fraction, in the sample. Removing these two data points, a slight increasing trend with radius is observed. This would indicate that the gravitational shocking experienced at lower Galactic radii causes more binaries to be destroyed or ejected. However, NGC 2158, with an R_{gc} of 13.5, is a high leverage point; its

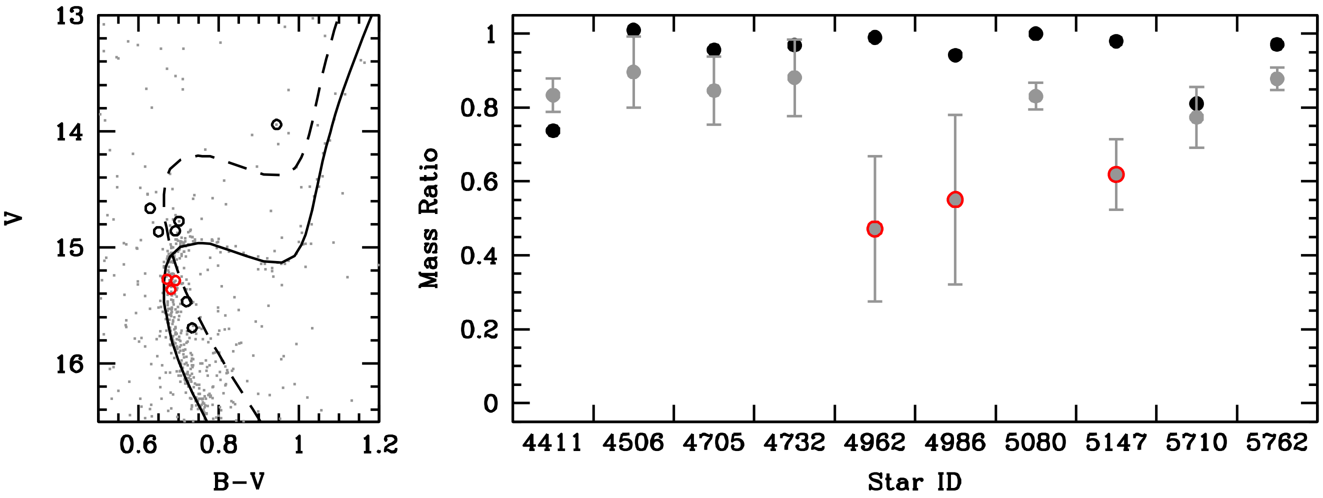

Figure 17. Left: NGC 188 CMD in $B-V$. The solid line is the isochrone used to generate models for BINOCS fitting. The dashed line is the equal-mass binary sequence. Black circles are double-lined binaries. Right: comparison of RV mass ratios (black) from Geller et al. (2009) to BINOCS (gray) for NGC 188 double-lined binaries. Stars outlined in red are those complicated by degeneracies close to the turnoff.

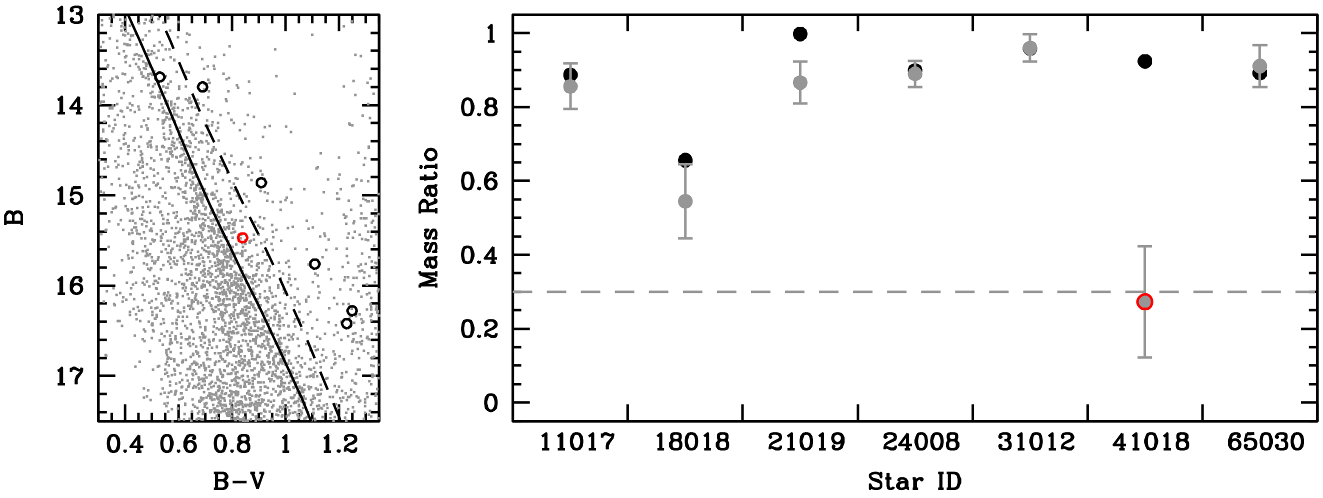

Figure 18. Same as Figure 17, but for NGC 2168. RV data are from Leiner et al. (2015). The stars outlined in red are below the $q \geqslant 0.3$ threshold level.

Table 8
Comparison of BINOCS and Geller et al. (2010) RV Multiplicity Results (as Shown in Figure 16)

	BINOCS		
	Single	Binary	Nonmember
Single	113 (45%)	98 (39%)	40 (16%)
Binary	8 (18%)	31 (69%)	6 (13%)

removal would result in there being no trend in R_{gc}. Additionally, the most central cluster is NGC 6791, with an age of 8 Gyr, while NGC 2158 has an age of 1.1 Gyr, an age difference that may explain the trend without R_{gc}.

As with the metallicity comparison, more clusters are needed to fill in the gaps in R_{gc}, disentangle correlations with age, and determine whether a trend truly exists. A more complete Figure 21 would allow the exploration of cluster–environment interactions and would inform cluster simulations on the correct treatment of tidal stripping events and other gravitational collisions.

Table 9
Comparison of BINOCS Membership to Gaia Membership

	BINOCS Member	BINOCS Nonmember
NGC 2682 ($H \geqslant 12$)		
Gaia member	354	60
Gaia nonmember	138	229
	NGC 2099 (all)	
Gaia member	886	82
Gaia nonmember	558	1152

8. Conclusions

Understanding main-sequence low-mass binary populations is essential for fully characterizing the masses and evolution of stellar clusters. The characteristics of binary populations, such as the mass function and radial distribution, are important for understanding the underlying physics of cluster evolution. It is well established that cluster stars, as well as high-mass binary systems, undergo mass segregation over time, but the extent

Table 10
Overall Binary Fractions for the Eight Clusters Considered in This Analysis

Cluster	Binary Fraction	Age (Gyr)	[Fe/H]	R_{gc} (kpc)	Number of Members	Mass Range ($M_\odot$)
NGC 188	0.44	6.30	−0.02	9.54	405	0.80–1.14
NGC 1960 (M36)	0.66	0.03	⋯	9.81	941	0.65–6.46
NGC 2099 (M37)	0.48	0.35	+0.08	9.88	1632	0.32–3.21
NGC 2158	0.49	1.10	−0.23	13.56	266	1.00–1.98
NGC 2168 (M35)	0.61	0.13	−0.21	9.37	2258	0.55–3.19
NGC 2420	0.41	2.00	−0.23	10.81	748	0.35–1.63
NGC 2682 (M67)	0.44	3.50	+0.01	9.11	642	0.19–1.40
NGC 6791	0.39	8.00	+0.38	8.11	524	0.89–1.16

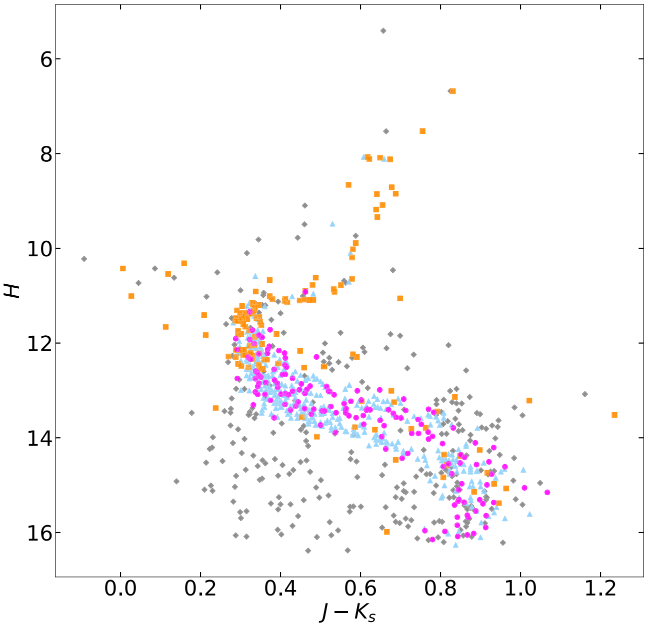

Figure 19. 2MASS CMD of cluster NGC 2682 stars analyzed by BINOCS with Gaia proper-motion-based membership data. Gray diamonds represent stars where both methods agree that they are nonmembers. Cyan triangles represent stars that are considered members with both the Gaia method and the BINOCS method. Orange squares represent stars that are considered members with Gaia and nonmembers with BINOCS. Magenta circles represent stars that are considered nonmembers with Gaia and members with BINOCS. Star counts in each category can be found in Table 9. For $H \geqslant 12$, where the BINOCS method is effective, the two membership methods agree for 74% of the stars.

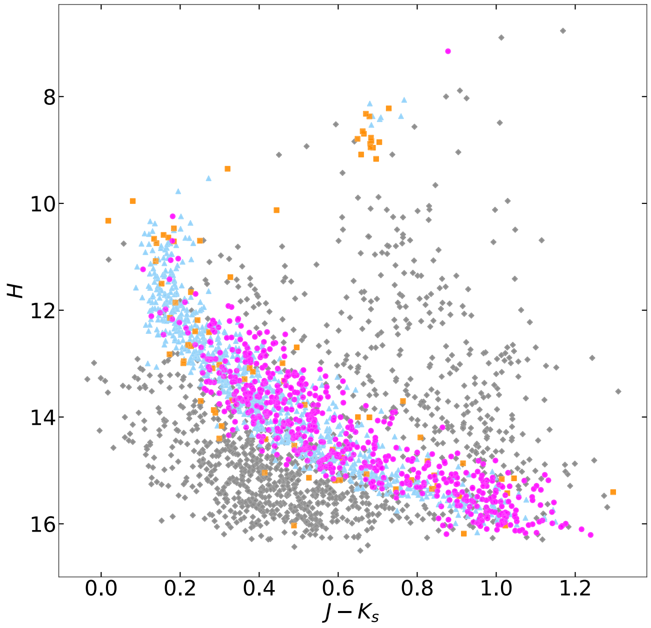

Figure 20. Same as Figure 19, but for the cluster NGC 2099. These two methods agree for 75% of the stars.

that this affects the low-mass binary population has not been fully explored. In this work:

1. We present new deep near-IR and mid-IR photometry for the open clusters NGC 2099 (M37) and NGC 2682 (M67). The NOAO/NEWFIRM photometry reaches a depth of (J,H,K_S = 18.6, 18.1, 17.8) for NGC 2099 and (J,H,K_S = 18.8, 19.0, 18.0) for NGC 2682. The Spitzer/IRAC photometry reaches a depth of ([3.6][4.5][5.8][8.0] = 18.0, 16.5, 14.6, 13.8) for NGC 2099 and ([3.6][4.5][5.8][8.0] = 18.5, 17.4, 15.0, 14.0) for NGC 2682.
2. We introduce the BINARY INFORMATION FROM OPEN CLUSTERS USING SEDS (BINOCS), a purely photometric method for determination of unresolved binaries and determination of the masses of both stars, for main-sequence stars with primary masses below the turnoff to 0.5 $M_\odot$ (2.5–0.5 $M_\odot$ for NGC 2099). We showed that the BINOCS method is a significant improvement over current binary detection techniques, requiring an order of magnitude less time, generating mass estimates on an order of magnitude more stars, and enabling quantitative exploration of faint binary systems, which are unreachable by RV studies. The BINOCS method allows for robust, quick binary classification that will become especially powerful as new all-sky surveys are released.
3. We tested the BINOCS code to ensure that it produced reasonable results for binary detection and mass determination, when compared to previously published studies based on multidecade RV work. Overall binary fractions can be computed quickly using BINOCS for clusters with sufficient photometry.
4. The results for NGC 188 are consistent with the result of Cohen et al. (2020), which compared to the BINOCS results as preliminarily presented in Frinchaboy & Thompson (2015).
5. We find a clear decrease in binary fraction with respect to cluster age, likely due to disruption of wide-binary systems in the cluster environment.

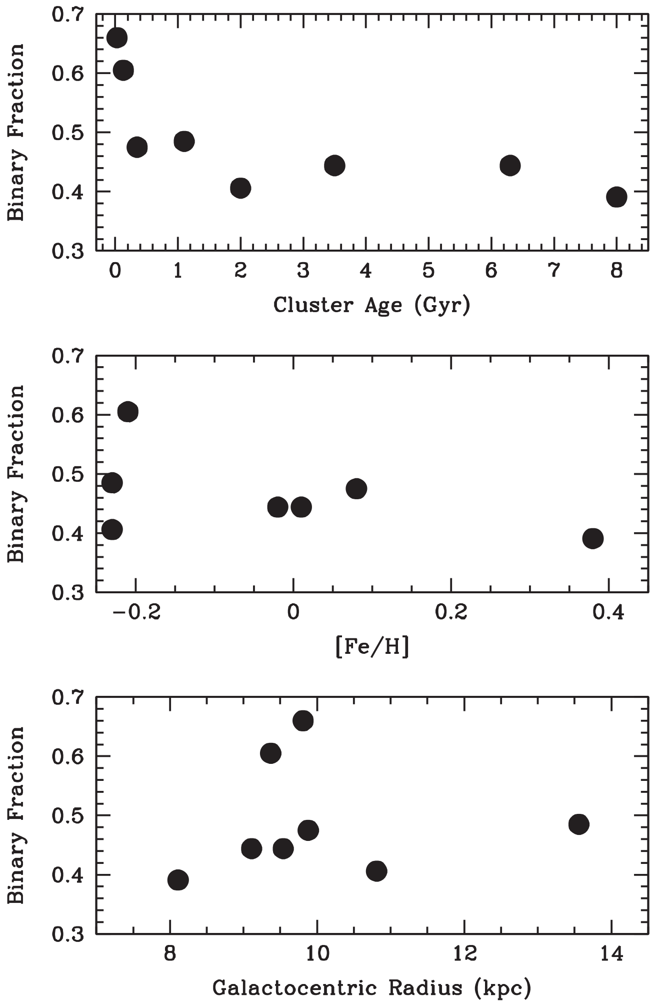

Figure 21. Top: overall cluster binary fraction, as a function of cluster age. Middle: overall cluster binary fraction, as a function of cluster [Fe/H]. Bottom: overall cluster binary fraction, as a function of cluster R_{gc}.

The authors would like to thank the referee for their patience and comments/suggestions that improved this paper.

The authors would like to acknowledge graduate thesis travel support from NOAO, as well as financial support from the Texas Space Grant Consortium and NSF-AST grant 1311835 and AST-1715662. Spitzer Cycle 3 observations were funded under NASA/JPL subaward grant GO-30800. The authors would especially like to thank the GLIMPSE team, specifically Brian Babbler and Marilyn Meade, for their contribution in modifying the GLIMPSE pipeline to handle our HDR IRAC data. The authors would also like to thank the Max-Planck-Institut für Astronomie (MPIA Heidelberg) for hosting P.M.F. and J.D. during the completion of this work.

This research uses services or data provided by the NOAO Science Archive. NOAO is operated by the Association of Universities for Research in Astronomy (AURA), Inc. under a cooperative agreement with the National Science Foundation. This work has also made use of the NASA/IPAC Infrared Science Archive, which is operated by the Jet Propulsion Laboratory, California Institute of Technology, under contract with the National Aeronautics and Space Administration.

ORCID iDs

Peter M. Frinchaboy https://orcid.org/0000-0002-0740-8346

References

Abazajian, K. N., Adelman-McCarthy, J. K., Agüeros, M. A., et al. 2009, ApJS, 182, 543
An, D., Pinsonneault, M. H., Masseron, T., et al. 2009, ApJ, 700, 523
Benjamin, R. A., Churchwell, E., Babler, B. L., et al. 2003, PASP, 115, 953
Bressan, A., Bressan, A., Marigo, P., et al. 2012, MNRAS, 427, 127
Carney, B. W., Lee, J.-W., & Dodson, B. 2005, AJ, 129, 656
Chambers, K. C., Magnier, E. A., Metcalfe, N., et al. 2016, arXiv:1612.05560
Churchwell, E., Babler, B. L., Meade, M. R., et al. 2009, PASP, 121, 213
Cohen, R. E., Geller, A. M., & von Hippel, T. 2020, AJ, 159, 11
de Grijs, R., Li, C., Zheng, Y., et al. 2013, ApJ, 765, 4
Dias, W. S., Alessi, B. S., Moitinho, A., & Lépine, J. R. D. 2002, A&A, 389, 871
Donor, J., Frinchaboy, P. M., Cunha, K., et al. 2018, AJ, 156, 142
Dotter, A., Chaboyer, B., Jevremović, D., et al. 2007, AJ, 134, 376
Elson, R. A. W., Sigurdsson, S., Davies, M., Hurley, J., & Gilmore, G. 1998, MNRAS, 300, 857
Fazio, G. G., Hora, J. L., Allen, L. E., et al. 2004, ApJS, 154, 10
Frinchaboy, P., & Thompson, B. 2015, in Proc. IAU Symp. 316, Formation, Evolution, and Survival of Massive Star Clusters, ed. C. Charbonnel & A. Nota (Cambridge: Cambridge Univ. Press), 04789
Gaia Collaboration, Brown, A. G. A., Vallenari, A., et al. 2018, A&A, 616, A1
Gaia Collaboration, Prusti, T., de Bruijne, J. H. J., et al. 2016, A&A, 595, A1
Geller, A. M., & Mathieu, R. D. 2012, AJ, 144, 54
Geller, A. M., Mathieu, R. D., Braden, E. K., et al. 2010, AJ, 139, 1383
Geller, A. M., Mathieu, R. D., Harris, H. C., & McClure, R. D. 2008, AJ, 135, 2264
Geller, A. M., Mathieu, R. D., Harris, H. C., & McClure, R. D. 2009, AJ, 137, 3743
Girardi, L., Bertelli, G., Bressan, A., et al. 2002, A&A, 391, 195
Hartman, J. D., Gaudi, B. S., Holman, M. J., et al. 2008, ApJ, 675, 1233
Hoffman, A. W., Corrales, E., Love, P. J., et al. 2004, Proc. SPIE, 5499, 59
Hole, K. T., Geller, A. M., Mathieu, R. D., et al. 2009, AJ, 138, 159
Hurley, J. R., Pols, O. R., Aarseth, S. J., et al. 2005, MNRAS, 363, 293
Hurley, J. R., Tout, C. A., Aarseth, S. J., et al. 2001, MNRAS, 323, 630
Ivezić, Ž, Kahn, S. M., Tyson, J. A., et al. 2019, ApJ, 873, 111
Leiner, E. M., Mathieu, R. D., Gosnell, N. M., et al. 2015, AJ, 150, 10
Lucas, P. W., Hoare, M. G., Longmore, A., et al. 2008, MNRAS, 391, 136
Mathieu, R. D., & Latham, D. W. 1986, AJ, 92, 1364
Mathieu, R. D., Latham, D. W., & Milone, A. E. 1997, in ASP Conf. Ser. 130, The Third Pacific Rim Conf. on Recent Development on Binary Star Research, ed. K.-C. Leung (San Fransisco, CA: ASP), 113
Milliman, K. E., Mathieu, R. D., Geller, A. M., et al. 2014, AJ, 148, 38
Milone, A. P., Piotto, G., Bedin, L. R., et al. 2012, A&A, 540, 16
Minniti, D., Lucas, P. W., Emerson, J. P., et al. 2010, NewA, 15, 433
Moyano Loyola, G. R. I., & Hurley, J. R. 2013, MNRAS, 434, 2509
Platais, I., Kozhurina-Platais, V., Mathieu, R. D., Girard, T. M., & van Altena, W. F. 2003, AJ, 126, 2922
Raghavan, D., & McAlister, H. A. 2009, AAS, 213, 330.04
Sanner, J., Altmann, M., Brunzendorf, J., & Geffert, M. 2000, A&A, 357, 471
Sawyer, D. G., Daly, P. N., Howell, S. B., Hunten, M. R., & Schweiker, H. 2010, Proc. SPIE, 7735, 77353A
Sharma, S., Pandey, A. K., Ogura, K., et al. 2006, AJ, 132, 1669
Skrutskie, M. F., Cutri, R. M., Stiening, R., et al. 2006, AJ, 131, 1163
Spergel, D., Gehrels, N., Breckinridge, J., et al. 2013, arXiv:1305.5422
Stetson, P. 1987, PASP, 99, 191
Stetson, P. B., McClure, R. D., & VandenBerg, D. A. 2004, PASP, 116, 1012
Swaters, R. A., Valdes, F., & Dickinson, M. E. 2009, in ASP Conf. Ser., 411, Astronomical Data Analysis Software and Systems XVIII, ed. D. A. Bohlender, D. Durand, & P. Dowler (San Francisco, CA: ASP), 506
Thompson, B., Frinchaboy, P., Kinemuchi, K., Sarajedini, A., & Cohen, R. 2014, AJ, 148, 85
Valle, G., Dell'Omodarme, M., Prada Moroni, P. G., Prada Moroni, P. G., & Degl'Innocenti, S. 2013, A&A, 549, 50
von Hippel, T., & Sarajedini, A. 1998, AJ, 116, 1789
Wright, E. L., Eisenhardt, P. R. M., Mainzer, A. K., et al. 2010, AJ, 140, 1868
Yadav, R. K. S., Bedin, L. R., Piotto, G., et al. 2008, A&A, 484, 609
York, D. G., Adelman, J., Adelman, J., et al. 2000, AJ, 120, 1579